

Long-Lived Ringing of Near-Extremal Kerr Black Holes Resonantly Driven by Extreme-Mass-Ratio Inspirals

Wen-Biao Han^{1,2,3,*}

¹*State Key Laboratory of Radio Astronomy and Technology,*

Shanghai Astronomical Observatory, CAS, 80 Nandan Road, Shanghai 200030, China

²*School of Fundamental Physics and Mathematical Sciences, Hangzhou Institute for Advanced Study,*

University of Chinese Academy of Sciences, Hangzhou 310024, China

³*School of Astronomy and Space Science, University of Chinese Academy of Sciences, Beijing 100049, China*

(Dated: June 17, 2026)

Near-extremal Kerr black holes support zero-damped modes (ZDMs), whose small time-domain damping rates make them long-lived probes of the near-horizon region. We show that bound extreme-mass-ratio inspirals (EMRIs) can resonantly drive this response in vacuum general relativity. Using frequency-domain Teukolsky amplitudes for eccentric-inclined Kerr geodesics, we identify a source-supported orbital harmonic whose real frequency falls within one pole half-width of the fundamental gravitational ZDM. In the complex response, the pole contribution is enhanced by this small half-width, while complex-response tomography recovers the independently computed Kerr pole from real-frequency orbital data. After subtracting the smooth non-pole component, the residual exhibits the phase winding of a coherent simple pole, with a pole contribution comparable to the smooth non-pole part of the EMRI-sourced Teukolsky amplitude. The driven branch also lies in the superradiant regime and carries negative horizon flux. These results establish a pole-resolved, resonantly driven ZDM response by EMRIs and make the recovered pole half-width a route to measuring the horizon surface gravity.

Introduction.— Extreme-mass-ratio inspirals (EMRIs) are among the cleanest probes of strong-field Kerr dynamics. A compact object orbiting a massive black hole radiates over 10^4 – 10^5 cycles, and its waveform encodes the three fundamental frequencies of generic bound Kerr geodesics [1–3],

$$\omega_{mnk} = m\Omega_\phi + n\Omega_r + k\Omega_\theta, \quad (1)$$

This discrete spectrum underlies black-hole mapping and precision tests of general relativity with space-based gravitational-wave detectors [4–8]. Most EMRI studies use these frequencies as probes of the background geometry and of the orbital radiation reaction. Here we ask a different question: can an EMRI harmonic act as a coherent external driver of a long-lived black-hole mode?

The relevant modes are the zero-damped quasinormal modes (ZDMs) of near-extremal Kerr black holes. Kerr perturbations are governed by the Teukolsky equation [9], and the associated quasinormal spectrum has been studied extensively since the classic work of Detweiler and Leaver [10–12]. Near extremality, the spectrum separates into damped modes and ZDMs, whose imaginary parts vanish in the extremal limit [13]. For a ZDM,

$$\omega_{\ell m N}^{\text{ZDM}} = m\Omega_H + \kappa(\varpi_{\ell m N} - i\Gamma_{\ell m N}) + O(\kappa^2), \quad (2)$$

where N is the overtone index and

$$\begin{aligned} \varpi_{\ell m N} &\equiv \lim_{\kappa \rightarrow 0} \frac{\text{Re} \omega_{\ell m N}^{\text{ZDM}} - m\Omega_H}{\kappa}, \\ \Gamma_{\ell m N} &\equiv \lim_{\kappa \rightarrow 0} \frac{-\text{Im} \omega_{\ell m N}^{\text{ZDM}}}{\kappa} > 0. \end{aligned} \quad (3)$$

Thus $\varpi_{\ell m N}$ is the dimensionless real-frequency offset from the superradiant bound, while $\Gamma_{\ell m N} > 0$ is the dimensionless damping coefficient. The physical damping rate, equivalently the pole half-width in a real-frequency response, is therefore

$$\gamma \equiv -\text{Im} \omega_{\ell m N}^{\text{ZDM}} = \kappa\Gamma_{\ell m N} + O(\kappa^2).$$

Here κ is the surface gravity of the Kerr horizon generator $\chi = \partial_t + \Omega_H \partial_\phi$; its explicit Kerr value is given below. Surface gravity is the intrinsic redshift and acceleration scale of a stationary horizon. It enters the black-hole first law, sets the Hawking temperature $T_H = \kappa/(2\pi)$ in units with $\hbar = k_B = 1$, and vanishes in the extremal limit [14, 15]. Equations (2) and (3) show that the same horizon scale controls the imaginary part of the ZDM frequency. Thus the ZDM sector is a natural candidate for horizon spectroscopy: measuring the pole half-width is, in principle, measuring a quantity controlled directly by the near-horizon geometry.

There are two reasons why an EMRI may access this sector more effectively than an ordinary perturbation. First, the source spectrum is not broadband noise but a set of long-lived, phase-coherent orbital harmonics. Second, near the horizon of a rapidly spinning black hole, three effects occur simultaneously: orbital harmonics approach the superradiant frequency scale $m\Omega_H$, source amplitudes can be enhanced near the separatrix, and the ZDM pole half-width shrinks with κ . These ingredients suggest a driven near-horizon resonance, but they also create an ambiguity. A large response near the separatrix need not be a QNM pole; it could be ordinary Teukolsky scattering, a smooth source enhancement, or superradiant horizon kinematics.

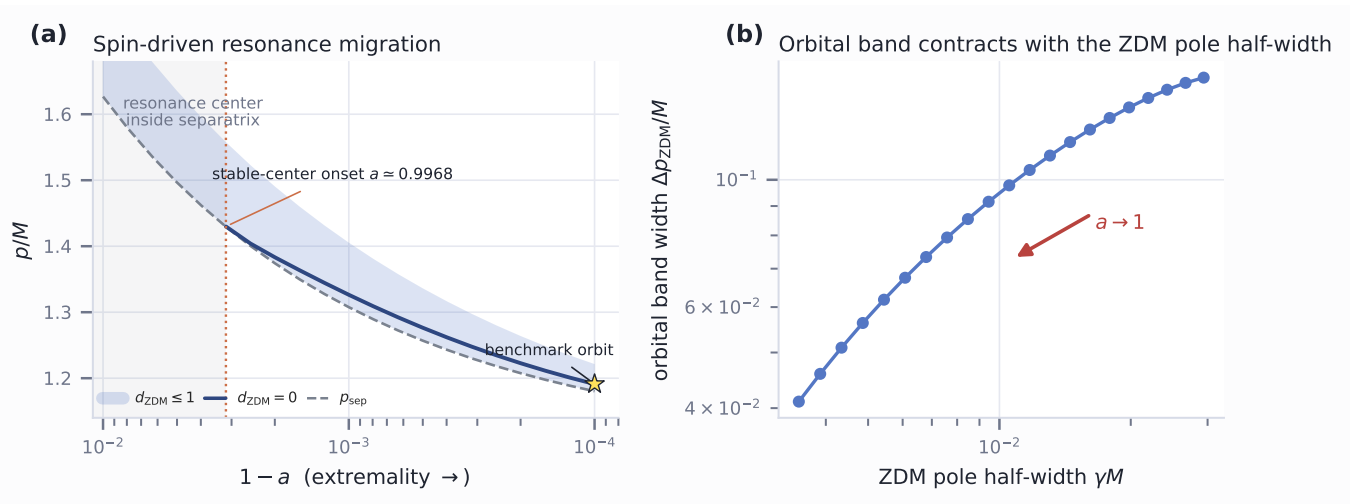


FIG. 1. **Spin-driven migration and contraction of the ZDM resonance channel.** Representative benchmark with $e = 0.1$, $\iota = 22^\circ$, and the $(m, n, k) = (2, 2, 1)$ harmonic. (a) Stable $d_{\text{ZDM}} \leq 1$ band versus $1 - a$. The solid curve satisfies $d_{\text{ZDM}} = 0$, shading denotes $d_{\text{ZDM}} \leq 1$, and the dashed curve is the inclined separatrix, where $d_{\text{ZDM}} = |\omega_{221} - \text{Re} \omega_{\text{ZDM}}|/\gamma$ and $\gamma = -\text{Im} \omega_{\text{ZDM}}$. In the gray region the exact resonance center lies inside the separatrix, although stable orbits still enter the $d_{\text{ZDM}} \leq 1$ band. The star marks the $a = 0.9999$ benchmark orbit used for the tomography and flux diagnostics. (b) Orbital band width $\Delta p_{\text{ZDM}} \equiv p_{\text{out}} - p_{\text{in}}$, the stable connected $d_{\text{ZDM}} \leq 1$ interval, versus the independent ZDM pole half-width.

Previous work found Kerr QNM “wiggles” in compact-object fields and self-forces, while direct tuning to QNM frequencies produced only small changes in the parameter ranges explored [16]. Superradiant horizon fluxes and tidal acceleration in EMRIs have also been studied [17–19]. These results motivate, but do not answer, the pole-specific question addressed here: whether the real-frequency EMRI response contains a recoverable and dynamically significant ZDM pole contribution.

To address this question, this Letter uses frequency-domain Teukolsky amplitudes for eccentric-inclined Kerr geodesics. The analysis has three steps. We first locate source-supported orbital regions whose harmonics enter one ZDM pole half-width. We then separate a shared simple-pole contribution from smooth non-pole terms using complex-response tomography. Finally, we evaluate the pole fraction and the associated horizon flux along the same branch. This keeps pole identification separate from ordinary source enhancement, smooth scattering, and superradiant horizon kinematics.

Orbital access to the ZDM pole half-width.— We set $G = c = M = 1$ and use

$$r_+ = 1 + \sqrt{1 - a^2}, \quad \Omega_H = \frac{a}{2r_+}, \quad \kappa = \frac{\sqrt{1 - a^2}}{2r_+}. \quad (4)$$

The calculation combines Kerr geodesic frequencies computed with `kerrgeopy` [1–3], independent Kerr QNM frequencies computed with `qnm` [20], and frequency-domain Teukolsky amplitudes and fluxes computed with `pybhpt` [9, 21]. As a representative benchmark, we use $e = 0.1$, the orbital harmonic $(m, n, k) = (2, 2, 1)$, and the gravitational mode $(s, \ell, m, N) = (-2, 2, 2, 0)$. The near-horizon

condition is $\omega_{221} \simeq m\Omega_H + \kappa\varpi_{220}$, with the common azimuthal number $m = 2$ for the orbital harmonic and the ZDM. This is the fundamental low-lying co-rotating gravitational ZDM sector; the low-order (n, k) prescreen and neighboring co-rotating sectors are summarized in the Supplemental Material.

For each spin we compute the independent ZDM on a continuous Kerr spin sequence and define the pole-half-width detuning

$$d_{\text{ZDM}} \equiv \frac{|\omega_{221} - \text{Re} \omega_{\text{ZDM}}|}{-\text{Im} \omega_{\text{ZDM}}}, \quad (5)$$

with $\omega_{\text{ZDM}} = \omega_{220}^{\text{ZDM}}(a)$ and $\gamma \equiv -\text{Im} \omega_{\text{ZDM}}$. The quantity d_{ZDM} is a detuning normalized by the pole half-width, not an arbitrary orbital tolerance. Near the ZDM pole the sourced response contains

$$Z_{\text{pole}}(\omega) = \frac{\mathcal{R}}{\omega - \omega_{\text{ZDM}}} = \frac{\mathcal{R}}{\Delta\omega + i\gamma},$$

$$\Delta\omega \equiv \omega_{221} - \text{Re} \omega_{\text{ZDM}},$$

so that

$$|Z_{\text{pole}}| = \frac{|\mathcal{R}|/\gamma}{\sqrt{1 + d_{\text{ZDM}}^2}}.$$

Thus $d_{\text{ZDM}} = 0$ is the real-frequency resonance center, while $d_{\text{ZDM}} \leq 1$ denotes the region within one pole half-width, where the driven pole amplitude remains within a factor $1/\sqrt{2}$ of its resonant value. The zero-damped nature of the mode enters through the small half-width $\gamma \propto \kappa$: as $a \rightarrow 1$, the resonance width narrows in frequency while the peak pole response scales as $1/\gamma$, provided the source projection \mathcal{R} remains nonzero and finite.

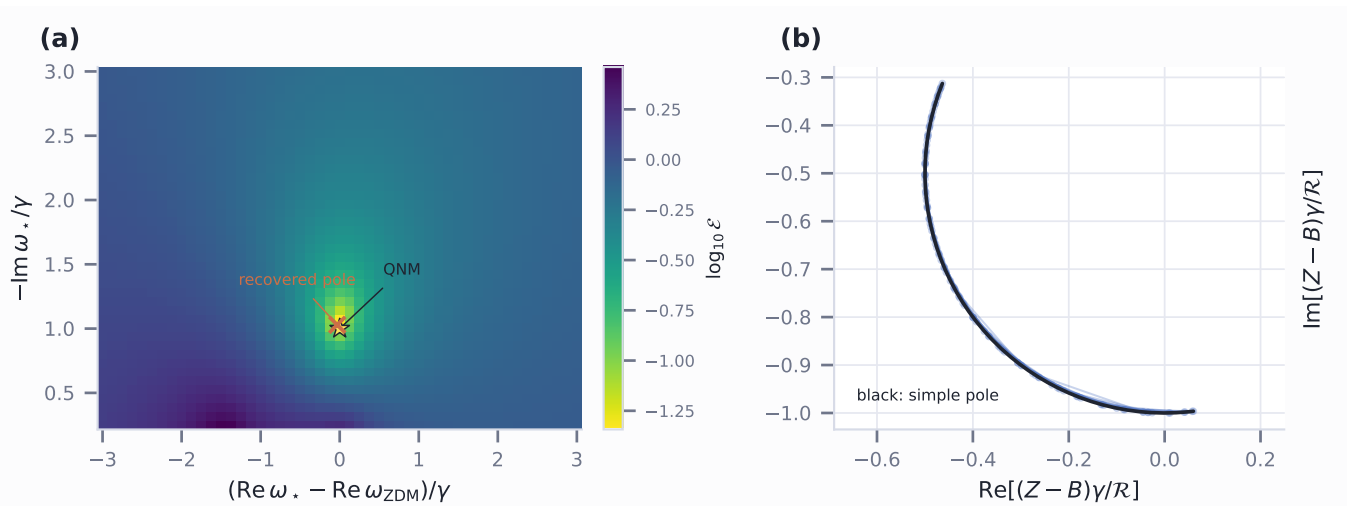


FIG. 2. **Complex-response tomography selects the independent ZDM pole.** Shared-pole test across multiple inclination cuts, each with its own smooth non-pole component and residue. (a) Joint normalized prediction error in the complex trial-pole plane; the star is the independent QNM and the cross is the recovered pole. (b) Residue-normalized, non-pole-subtracted trajectories for all inclination cuts compared with a simple-pole response (black).

Figure 1 summarizes the orbital origin and near-extremal scaling of this resonance channel. The real-frequency center $d_{\text{ZDM}} = 0$ migrates inward as $a \rightarrow 1$ and remains close to the inclined separatrix once a stable exact crossing appears. The shaded region is the set of stable orbits whose source harmonic lies within one ZDM pole half-width, $d_{\text{ZDM}} \leq 1$. Here the inclined separatrix $p_{\text{sep}}(e, \iota, a)$ denotes the last stable orbit boundary between stable bound eccentric-inclined geodesics and plunging motion; stable orbits require $p > p_{\text{sep}}$. Near an unclipped stable crossing at $p = p_c$,

$$\omega_{221}(p) \simeq \text{Re } \omega_{\text{ZDM}} + \partial_p \omega_{221}|_{p_c} (p - p_c),$$

so the corresponding orbital interval obeys

$$\Delta p_{\text{ZDM}} \sim \frac{2\gamma}{|\partial_p \omega_{221}|_{p_c}}.$$

When the inner side of this interval lies inside the separatrix, the stable band is clipped at p_{sep} . Thus the orbital access window should contract as the ZDM pole half-width narrows, modulo the local orbital-frequency gradient and separatrix clipping.

Figure 1(b) verifies this expectation directly. Along the fixed-orbit family the measured stable band width $\Delta p_{\text{ZDM}} \equiv p_{\text{out}} - p_{\text{in}}$, where $[p_{\text{in}}, p_{\text{out}}]$ is the connected stable interval satisfying $d_{\text{ZDM}} \leq 1$, contracts with the independently computed pole half-width. Since the same ZDM branch has $\gamma \propto \kappa$, the resonance channel is tied to the surface-gravity scale of the near-horizon pole, rather than to a freely chosen orbital window. Descriptive fit coefficients are given in the Supplemental Material.

Complex-pole tomography.— On each fixed-inclination cut, we write the corrected infinity amplitude as a smooth

non-pole component plus a candidate pole term,

$$Z_i^\infty(\omega) = B_i(\omega) + Z_{i,\text{pole}}^\infty(\omega), \quad Z_{i,\text{pole}}^\infty(\omega) = \frac{\mathcal{R}_i}{\omega - \omega_*}, \quad (6)$$

where $B_i(\omega) \equiv Z_{i,\text{np}}^\infty$ denotes the smooth non-pole component of the EMRI-sourced Teukolsky amplitude on inclination cut i . It absorbs the direct and non-resonant scattering response of the source, as well as other slowly varying non-pole contributions in the local frequency window.

To implement this separation, we approximate the smooth term locally by

$$B_i(\omega) = \sum_{j=0}^2 c_{ij} x^j, \quad (7)$$

where x is a centered and scaled real frequency. This quadratic form is a local nuisance expansion, not a global model of the EMRI response. Each inclination cut has its own B_i and \mathcal{R}_i , while the complex pole frequency ω_* is shared by all cuts. An equal-complexity cubic polynomial supplies the no-pole control. We compare the models by leave-one-out complex prediction error and define the joint score

$$\mathcal{E}(\omega_*) = \exp \left[\frac{1}{N_t} \sum_i \ln \frac{\epsilon_{\text{pole},i}(\omega_*)}{\epsilon_{\text{cubic},i}} \right]. \quad (8)$$

This normalization prevents high-amplitude cuts from determining the pole. The purpose of this tomography is to decide whether the frequency access in Fig. 1 corresponds to an actual pole of the sourced EMRI response, rather

than to a smooth source enhancement or a single fine-tuned orbital cut. The test is deliberately overconstrained: each inclination cut has its own smooth non-pole component and residue, but all cuts must share one complex pole.

Figure 2(a) gives the existence and localization test. The joint prediction error has a compact minimum at the independently computed ZDM, and allowing the pole to move gives

$$\frac{\operatorname{Re}(\omega_* - \omega_{\text{ZDM}})}{\gamma} = -0.0313, \quad \frac{-\operatorname{Im}\omega_*}{\gamma} = 1.029. \quad (9)$$

Thus the pole can be recovered from real-frequency EMRI data without imposing the QNM frequency as an input. The independent pole gives $\mathcal{E} = 0.0529$; deliberate frequency shifts, halving or doubling the pole half-width, and the upper-half-plane conjugate yield much larger errors, while the minimum is unchanged when any one of the 12 inclination cuts is removed. The one-dimensional coordinate slices, shown in the Supplemental Material, verify that both the real part and the pole half-width are selected. After subtracting the fitted smooth component and normalizing by the residue, all cuts follow the phase winding of a simple pole, $1/(\omega - \omega_{\text{ZDM}})$ [Fig. 2(b)]. These signatures establish that the EMRI response contains a coherent, accessible ZDM pole contribution; its quantitative strength relative to the smooth non-pole component is measured next.

Pole fraction and flux.— To quantify dynamical importance within Eq. (6), we define

$$\mathcal{P} = \frac{|Z_{\text{pole}}|}{|B|} = \frac{|\mathcal{R}/(\omega - \omega_{\text{ZDM}})|}{|B(\omega)|}. \quad (10)$$

Figure 3 shows that the recovered pole is not merely identifiable, but dynamically relevant. Across all tomography cuts, \mathcal{P} increases systematically as d_{ZDM} decreases, demonstrating that the enhanced coherent component is tied to the ZDM pole half-width rather than to a monotonic inward source enhancement. The full sample has median $\mathcal{P} = 0.632$ and maximum 0.887: the pole remains comparable to, but does not dominate, the smooth non-pole response. This is consistent with the absence of a sharp Lorentzian feature in the total amplitude.

The net energy flux gives a related energy-budget diagnostic. We sum over spheroidal and orbital harmonics and evaluate

$$\eta_{\text{tot}} = \frac{|\dot{E}_H^{\text{tot}}|}{\dot{E}_\infty^{\text{tot}}}. \quad (11)$$

The horizon flux remains negative throughout the common-truncation scan and varies smoothly through the real-frequency crossing. A higher-order calculation with $\ell \leq 10$, $|k| \leq 6$, and $|n| \leq 30$ gives $\eta_{\text{tot}} = 0.184$ at the high-order anchor (see Supplemental Material). Thus the ZDM channel produces an $\mathcal{O}(10\%)$ superradiant

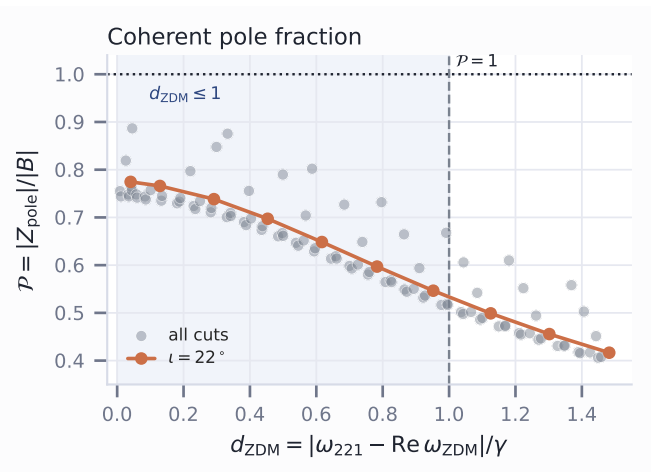


FIG. 3. **Coherent pole fraction.** Pole-to-non-pole ratio for the $a = 0.9999$, $e = 0.1$ tomography sample, plotted directly against the detuning normalized by the pole half-width. Gray points show all inclination cuts; orange points highlight the benchmark $\iota = 22^\circ$ cut. The shaded region is the $d_{\text{ZDM}} \leq 1$ interval, and the dotted horizontal line marks pole–non-pole parity.

correction to the EMRI energy budget, while its smooth variation explains why the pole is most cleanly resolved in the complex amplitude rather than in a flux peak.

As a consistency check on the driven response, compare the free decay time with the EMRI frequency-sweep time. In the phase frame of the orbital harmonic, the fitted pole term obeys the reduced driven-mode equation

$$\dot{A} + (\gamma - i\delta)A = -i\mathcal{R}, \quad \delta = \omega_{221} - \operatorname{Re}\omega_{\text{ZDM}}. \quad (12)$$

Besides $\tau_{\text{ZDM}} = \gamma^{-1}$, define the local time to sweep by one pole half-width and its ratio to the damping time,

$$\tau_{\text{sweep}} = \frac{\gamma}{|\delta|}, \quad \frac{\tau_{\text{sweep}}}{\tau_{\text{ZDM}}} = \frac{\gamma^2}{|\delta|^2}. \quad (13)$$

For $\mu/M = 10^{-5}$, a reduced inspiral driven by the candidate harmonic gives $|\delta| = 4.69 \times 10^{-10} M^{-2}$ at the crossing. Thus

$$\tau_{\text{ZDM}} = 288.3M, \quad (14)$$

$$\tau_{\text{sweep}} = 7.40 \times 10^6 M = 2.57 \times 10^4 \tau_{\text{ZDM}}. \quad (15)$$

For a $10^6 M_\odot$ primary these are 23.7 minutes and 1.15 yr, respectively. Since $|\delta| \propto \mu/M$ in the adiabatic limit, the hierarchy grows inversely with mass ratio. The numerical envelope follows its instantaneous forced solution to within 4.9×10^{-4} on the sampled track. The large separation in Eq. (15) therefore supports a quasi-steady, coherently driven ZDM rather than a short transient or an isolated waveform spike. A quantitative waveform or dephasing prediction would require a full multimode inspiral through the narrow ZDM region.

Discussion.— The calculation establishes a specific route by which an EMRI can drive a long-lived near-horizon ZDM response. A discrete orbital harmonic enters one pole half-width of the fundamental co-rotating ZDM; the corresponding access window contracts with the independently computed pole half-width; complex-response tomography then recovers the same pole from real-frequency source data; and after subtracting the smooth non-pole response, the residual follows the phase winding of a simple pole with $\mathcal{P} = O(1)$. Because $\gamma \propto \kappa$, the recovered pole half-width connects this driven ZDM response to the horizon surface gravity. The physical point is that an EMRI can act not only as a long-duration mapper of Kerr orbital frequencies, but also as a coherent external driver of the near-horizon mode spectrum. The result is therefore not simply a large Teukolsky amplitude near the separatrix, nor a kinematic superradiant flux effect, but a pole-resolved response of the near-extremal horizon spectrum.

Superradiant braking is a related energy-budget consequence, not the pole-identification criterion. It does not follow that the flux must peak: the complex interference between pole and the smooth non-pole component is lost in $|Z^\infty|^2$, while the horizon flux also contains smooth superradiant factors. The timescale estimate above indicates that the candidate is driven quasi-steadily across the pole half-width, but turning this pole-resolved response into an observable waveform prediction requires projecting the source onto the QNM with a properly normalized Kerr Green-function residue [22] and evolving a full multimode inspiral through the near-resonant region. With such a calibrated waveform model, recovering the pole half-width from an observed EMRI would provide a dynamical measurement of the horizon surface gravity, rather than only a consistency test of the Kerr orbital frequency map.

Acknowledgments.— This work was supported by the National Science and Technology Major Project of China (No. 2024ZD1100601), the National Key R&D Program of China (No. 2021YFC2203002) and the NSFC (National Natural Science Foundation of China) No. 12473075.

* wbhan@shao.ac.cn

- [1] W. Schmidt, Celestial mechanics in kerr spacetime, *Classical and Quantum Gravity* **19**, 2743 (2002), arXiv:gr-qc/0202090.
- [2] S. Drasco and S. A. Hughes, Rotating black hole orbit functionals in the frequency domain, *Physical Review D* **69**, 044015 (2004), arXiv:astro-ph/0308479.
- [3] R. Fujita and W. Hikida, Analytical solutions of bound timelike geodesic orbits in kerr spacetime, *Classical and Quantum Gravity* **26**, 135002 (2009), arXiv:0906.1420 [gr-qc].
- [4] F. D. Ryan, Gravitational waves from the inspiral of a compact object into a massive, axisymmetric body with arbitrary multipole moments, *Physical Review D* **52**, 5707 (1995).
- [5] L. Barack and C. Cutler, LISA capture sources: Approximate waveforms, signal-to-noise ratios, and parameter estimation accuracy, *Physical Review D* **69**, 082005 (2004), arXiv:gr-qc/0310125.
- [6] J. R. Gair, M. Vallisneri, S. L. Larson, and J. G. Baker, Testing general relativity with low-frequency, space-based gravitational-wave detectors, *Living Reviews in Relativity* **16**, 7 (2013), arXiv:1212.5575 [gr-qc].
- [7] P. Amaro-Seoane *et al.*, Laser interferometer space antenna, arXiv e-prints (2017), arXiv:1702.00786 [astro-ph.IM].
- [8] S. Babak, J. Gair, A. Sesana, E. Barausse, C. F. Sopuerta, C. P. L. Berry, E. Berti, P. Amaro-Seoane, A. Petiteau, and A. Klein, Science with the space-based interferometer LISA. v. extreme mass-ratio inspirals, *Physical Review D* **95**, 103012 (2017), arXiv:1703.09722 [gr-qc].
- [9] S. A. Teukolsky, Perturbations of a rotating black hole. i. fundamental equations for gravitational, electromagnetic, and neutrino-field perturbations, *The Astrophysical Journal* **185**, 635 (1973).
- [10] S. Detweiler, Black holes and gravitational waves. iii. the resonant frequencies of rotating holes, *The Astrophysical Journal* **239**, 292 (1980).
- [11] E. W. Leaver, An analytic representation for the quasinormal modes of kerr black holes, *Proceedings of the Royal Society of London. Series A* **402**, 285 (1985).
- [12] E. Berti, V. Cardoso, and A. O. Starinets, Quasinormal modes of black holes and black branes, *Classical and Quantum Gravity* **26**, 163001 (2009), arXiv:0905.2975 [gr-qc].
- [13] H. Yang, A. Zimmerman, A. Zenginoğlu, F. Zhang, E. Berti, and Y. Chen, Quasinormal modes of nearly extremal kerr spacetimes: spectrum bifurcation and power-law ringdown, *Physical Review D* **87**, 041502 (2013), arXiv:1212.3271 [gr-qc].
- [14] J. M. Bardeen, B. Carter, and S. W. Hawking, The four laws of black hole mechanics, *Communications in Mathematical Physics* **31**, 161 (1973).
- [15] S. W. Hawking, Particle creation by black holes, *Communications in Mathematical Physics* **43**, 199 (1975).
- [16] J. Thornburg, B. Wardell, and M. van de Meent, Excitation of kerr quasinormal modes in extreme-mass-ratio inspirals, *Physical Review Research* **2**, 013365 (2020), arXiv:1906.06791 [gr-qc].
- [17] W. H. Press and S. A. Teukolsky, Floating orbits, superradiant scattering and the black-hole bomb, *Nature* **238**, 211 (1972).
- [18] S. A. Teukolsky and W. H. Press, Perturbations of a rotating black hole. iii. interaction of the hole with gravitational and electromagnetic radiation, *The Astrophysical Journal* **193**, 443 (1974).
- [19] S. A. Hughes, Evolution of circular, nonequatorial orbits of kerr black holes due to gravitational-wave emission, *Physical Review D* **61**, 084004 (2000), arXiv:gr-qc/9910091.
- [20] G. B. Cook and M. Zaltskiy, qnm: Python routines for kerr quasinormal modes (2020).
- [21] Black Hole Perturbation Toolkit contributors, pybhpt: Python tools for black-hole perturbation theory (2026).
- [22] S. R. Green, S. Hollands, L. Sberna, V. Toomani, and P. Zimmerman, Conserved currents for kerr and orthogonality of quasinormal modes, *Physical Review D* **107**, 064030 (2023), arXiv:2210.15935 [gr-qc].

SUPPLEMENTAL MATERIAL

BRANCH SELECTION AND NEAR-HORIZON CONTINUATION

The low-order prescreen tests whether a sourced EMRI harmonic can enter one ZDM pole half-width in the stable region outside the inclined separatrix. The scan covers positive and negative radial and polar harmonics (n, k) , evaluates the scaled detuning

$$d_{\text{ZDM}} = \frac{|\omega_{mnk} - \text{Re}\omega_{\text{ZDM}}|}{\gamma}, \quad (\text{S1})$$

and ranks source-supported samples by $S_\infty = |Z^\infty|^2 / (1 + d_{\text{ZDM}}^2)$. The selected $(m, n, k) = (2, 2, 1)$ branch is then followed along a continuous near-extremal spin sequence. At each spin we solve for the outermost stable root of $\omega_{221} = \text{Re}\omega_{\text{ZDM}}$; when the inner $d_{\text{ZDM}} = 1$ boundary is unstable, the stable portion of the band is truncated at the inclined separatrix.

Table SI shows that the selected $(n, k) = (2, 1)$ branch is simultaneously close to the fundamental ZDM pole, source supported, and in the superradiant regime. Neighboring co-rotating sectors for the same orbital harmonic are less competitive: the fundamental $(\ell, m, N) = (2, 2, 0)$ sector lies within the pole half-width, whereas the nearby $\ell = 3$ and $\ell = 4$ sectors are several pole half-widths away at the source-supported point and have weaker source support. The table is a branch-selection diagnostic rather than a uniqueness claim.

Figure S1 follows the selected sourced track from $a = 0.99$ to $a = 0.9999$ and inclinations 23° – 25° . The track remains within $1.3 \times 10^{-2}M$ of the inclined separatrix while preserving stable access to the ZDM pole half-width. It is therefore the numerical continuation behind the near-extremal branch used in the Letter.

NUMERICAL ACCURACY CHECK

The pole tomography uses complex Z^∞ values from the high-resolution $a = 0.9999$, $e = 0.1$, $(m, n, k) = (2, 2, 1)$ grid near the selected branch. Table SII reports the `pybhpt` radial-solver precision diagnostics for the infinity and horizon amplitudes in this grid. These diagnostics are several orders of magnitude below the order-unity changes tested by the pole/non-pole tomography.

The nearest sample to the benchmark crossing, $(p, \iota) = (1.190, 22^\circ)$, has $d_{\text{ZDM}} = 4.06 \times 10^{-2}$, $|Z^\infty|^2 = 2.31 \times 10^5$, $\epsilon_\infty = 2.22 \times 10^{-13}$, and $\epsilon_H = 2.00 \times 10^{-13}$. The same sample has negative horizon flux, so it lies in the superradiant regime used in the main analysis.

POLE TOMOGRAPHY AND POLE FRACTION

On every fixed-inclination cut we fit a quadratic smooth non-pole component plus the independent ZDM pole and compare it with an equal-complexity cubic polynomial. The comparison uses leave-one-out complex-amplitude RMSE. Varying the fit window in d_{ZDM} and the non-pole order preserves the preference for the fixed-pole model. The fitted residue includes the Green-function residue, source projection, and normalization conventions; consequently, the pole fraction quoted below is a local response diagnostic, not an independently normalized QNM excitation coefficient.

The joint tomography uses 110 samples on 12 inclination cuts, each containing 6–10 real-frequency points. At the independent ZDM, the normalized joint leave-one-out score is 0.0528972. The freely recovered pole has $\Delta\omega_R/\gamma = -0.03125$, half-width ratio 1.02917, and score 0.0224826. Frequency shifts by one pole half-width, halving or doubling the pole half-width, and reflection into the upper half plane all perform substantially worse. A leave-one-inclination-out jackknife returns the same grid minimum for all 12 omissions.

Figure S2 displays the pole-recovery controls. The cross-validation landscape and one-dimensional slices test the two coordinates of the complex pole; the jackknife tests that no single inclination cut fixes the result; and the phase-winding panel checks the residue-normalized simple-pole behavior after smooth-background subtraction.

For each local fit we evaluate

$$\mathcal{P} = \frac{|\mathcal{R}/(\omega - \omega_{\text{ZDM}})|}{|B(\omega)|}. \quad (\text{S2})$$

The full sample has median $\mathcal{P} = 0.632195$, maximum 0.886629, and no sample with $\mathcal{P} > 1$. For $d_{\text{ZDM}} < 0.1$, the range is 0.738–0.887, and the rank correlation between \mathcal{P} and d_{ZDM} is -0.923 . The pole contribution is therefore comparable to, but not larger than, the fitted smooth non-pole part in the local response model.

ECCENTRICITY AND INCLINATION SURVEY

The fixed-spin survey at $a = 0.9999$ spans $0.01 \leq e \leq 0.50$ and $5^\circ \leq \iota \leq 30^\circ$ for the selected orbital harmonic. It checks whether nearby eccentric and inclined geodesics retain stable access to the same near-ZDM condition. The scan is not a universality statement over all EMRIs; it tests the local robustness of the representative branch used in the Letter.

Figure S3 shows that the near-ZDM band persists over nonzero inclinations and across the sampled eccentricities, while the source strength and separatrix distance vary across the scan.

TABLE SI. Low-order sourced prescreen at $a = 0.99$, $e = 0.1$, $m = 2$, for the fundamental gravitational sector $(s, \ell, m, N) = (-2, 2, 2, 0)$. Here d_{\min} is the minimum detuning normalized by the pole half-width on the coarse p -inclination grid, d_T is the corresponding detuning at the Teukolsky source-supported sample, and $S_T \equiv |Z^\infty|^2/(1 + d_T^2)$. The column $\dot{E}_H < 0$ refers to the same Teukolsky sample. The daggered \mathcal{P}_{\max} is the maximum pole fraction from the full $a = 0.9999$ tomography of the selected branch; entries marked by dashes were not subjected to pole/non-pole tomography.

(n, k)	d_{\min}	d_T	\mathcal{P}_{\max}	$ Z^\infty ^2$	S_T	$\dot{E}_H < 0$
(1, 1)	8.9×10^{-2}	0.619	–	1.83	1.32	yes
(2, 1)	3.7×10^{-4}	0.299	0.887 [†]	1.34	1.23	yes
(0, 1)	5.8×10^{-1}	0.579	–	2.31×10^{-1}	1.73×10^{-1}	yes
(2, 2)	1.0×10^{-3}	0.251	–	9.98×10^{-2}	9.39×10^{-2}	yes
(0, 2)	5.0×10^{-3}	0.152	–	3.36×10^{-2}	3.28×10^{-2}	no
(-2, 2)	2.0×10^{-3}	0.502	–	2.04×10^{-2}	1.63×10^{-2}	yes
(1, 2)	1.8×10^{-2}	0.235	–	1.18×10^{-2}	1.12×10^{-2}	yes
(-1, 2)	9.2×10^{-3}	0.113	–	1.54×10^{-4}	1.52×10^{-4}	no

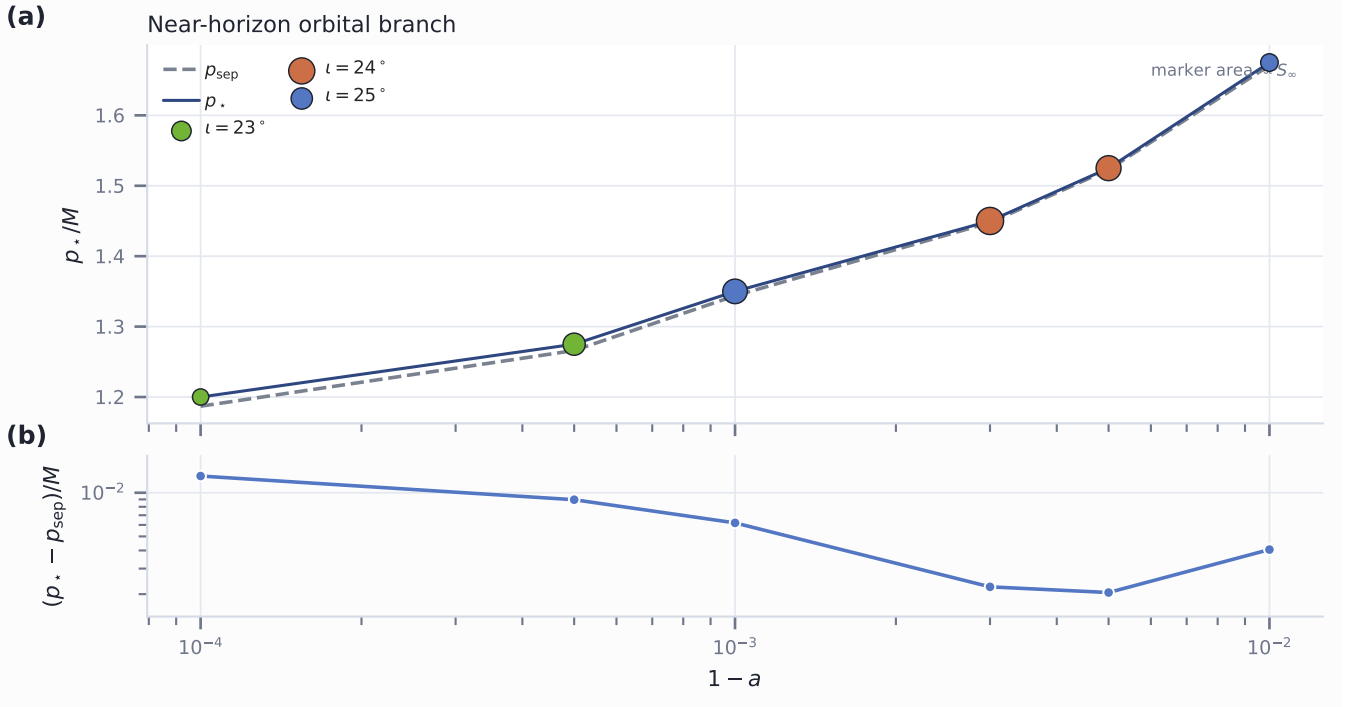


FIG. S1. Source-supported spin branch. Top: selected semi-latus rectum and inclined separatrix, with marker area proportional to S_∞ and color denoting inclination. Bottom: distance of the selected source from the separatrix.

TABLE SII. Numerical precision diagnostics for the high-resolution single-mode Teukolsky grid used in the pole tomography. The entries give the median and maximum diagnostic values for the infinity and horizon amplitudes.

Sample	Channel	N	median/max
finite grid	∞	262	$1.9 \times 10^{-14}/5.6 \times 10^{-12}$
finite grid	H	262	$1.6 \times 10^{-14}/4.7 \times 10^{-12}$
$d_{\text{ZDM}} \leq 1$	∞	129	$2.7 \times 10^{-14}/5.6 \times 10^{-12}$
$d_{\text{ZDM}} \leq 1$	H	129	$2.4 \times 10^{-14}/4.7 \times 10^{-12}$
$\iota = 22^\circ$ cut	∞	16	$1.5 \times 10^{-14}/8.1 \times 10^{-13}$
$\iota = 22^\circ$ cut	H	16	$1.4 \times 10^{-14}/7.2 \times 10^{-13}$

The complex response selects the independently computed Kerr ZDM pole

$a = 0.9999$; shared pole, independent quadratic backgrounds and residues; score is geometric-mean LOOCV error relative to equal-complexity cubics.

Independent ZDM score=0.0529; tomography minimum $\Delta\omega_R/\gamma = -0.03$, $\gamma./\gamma = 1.03$.

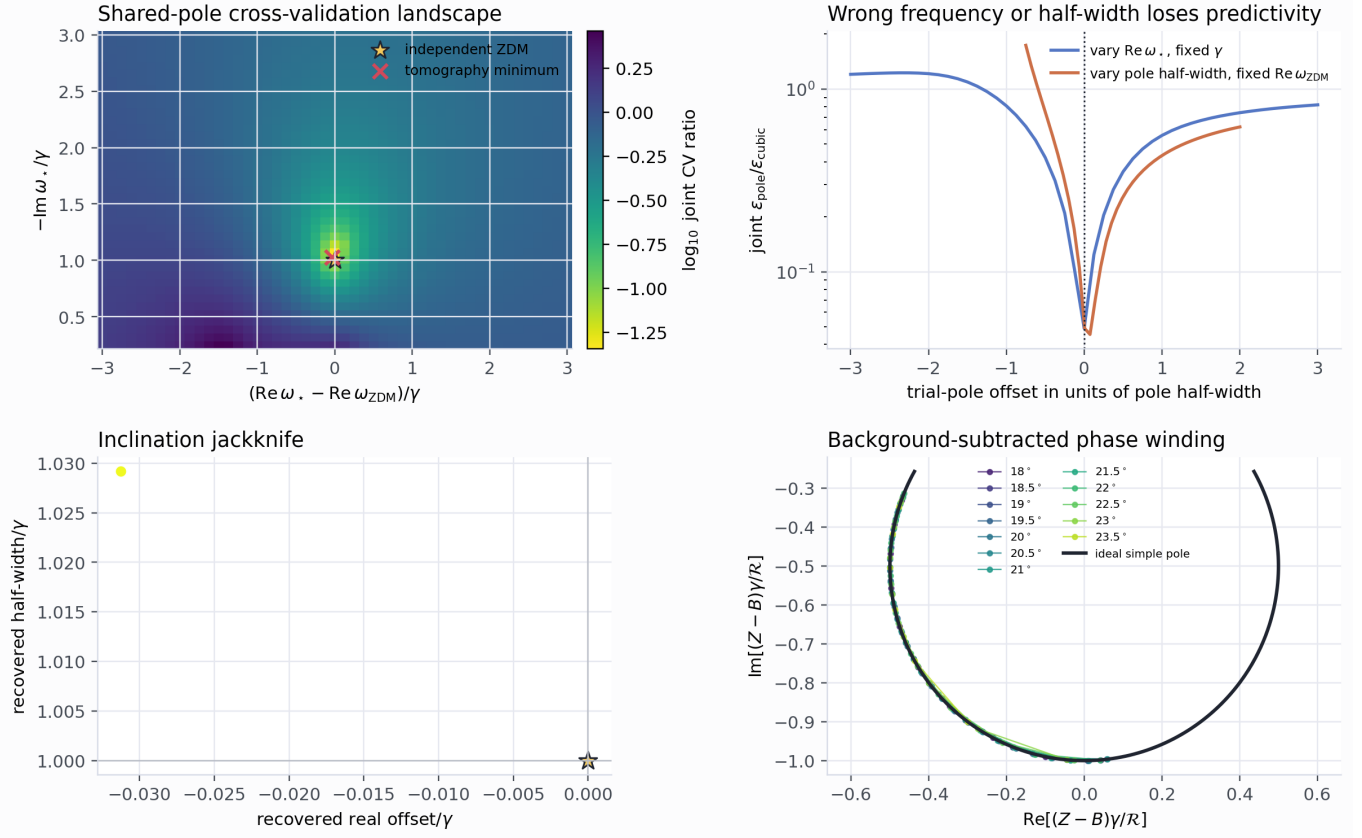


FIG. S2. Tomography robustness diagnostics. Top left: joint leave-one-out cross-validation score in the complex trial-pole plane; the star marks the independently computed ZDM and the cross marks the best recovered pole. Top right: one-dimensional coordinate slices showing that shifting the real frequency or changing the pole half-width worsens the prediction error. Bottom left: leave-one-inclination-out jackknife of the recovered pole coordinates, testing that no single inclination cut fixes the result. Bottom right: residue-normalized, background-subtracted phase winding for each inclination cut compared with the ideal simple-pole trajectory. Together the panels show that the complex response selects the independent Kerr ZDM pole.

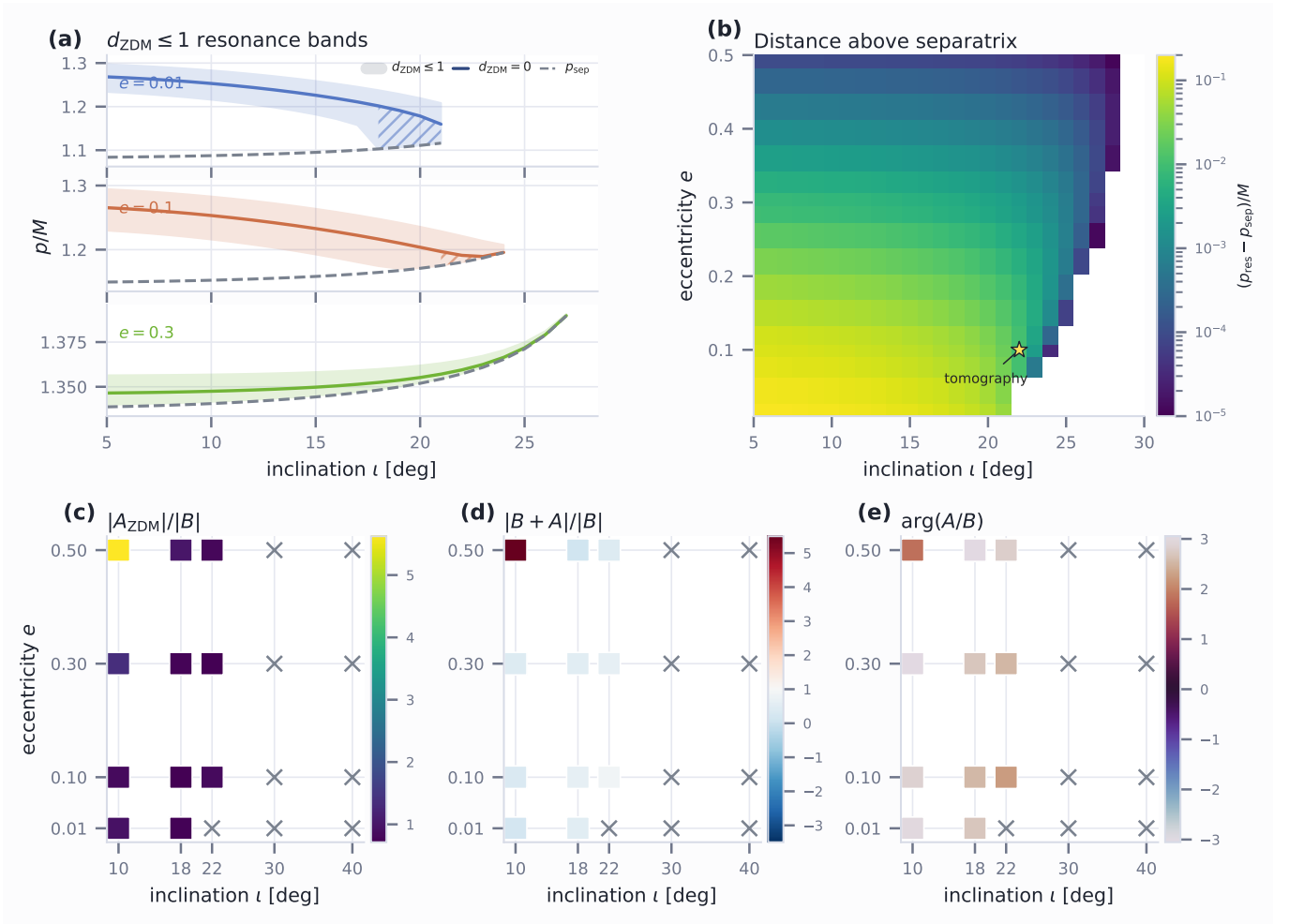


FIG. S3. Eccentricity–inclination survey at $a = 0.9999$. (a) Connected $d_{\text{ZDM}} \leq 1$ bands for representative eccentricities, with hatching marking separatrix-truncated bands. (b) Stable resonance distance above the separatrix over the scan. (c)–(e) Source projection, coherent gain, and pole–background phase at stable resonance roots; crosses mark samples without a usable stable root or local fit.